Applied Catalysis B: Environmental 303 (2022) 120920

Contents lists available at ScienceDirect

Applied Catalysis B: Environmental

journal homepage: www.elsevier.com/locate/apcatb

In-situ enhanced catalytic reforming behavior of cobalt-based materials with inherent zero-valent aluminum in spent lithium ion batteries

Jiadong Yu [a], Shujuan Zou [a], Guiyin Xu [b], Lili Liu [a], Ming Zhao [a], Jinhui Li [a,*]

[a] State Key Joint Laboratory of Environment Simulation and Pollution Control, School of Environment, Tsinghua University, Beijing 100084, China
[b] Department of Nuclear Science and Engineering and Department of Materials Science and Engineering, Massachusetts Institute of Technology, Cambridge, MA 02139, USA

ARTICLE INFO

Keywords:
Spent lithium ion batteries
In-situ
Catalytic behavior
Hydrogen evolution reaction
CO_2 conversion

ABSTRACT

As a renewable energy source, hydrogen production from biomass pyrolysis is one of the effective ways to promote global sustainable development. Herein, the inherent Al foils and typical $LiCoO_2$ cathodes in spent lithium ion batteries are jointly employed as the catalyst to reform sawdust pyrolysis gas to produce hydrogen-rich synthesis gas. It is the introduction of Al element that triggers the in-situ atomic replacement reaction to immobilize volatile lithium, thereby inducing the formation of a similar Li-CO_2 battery system, which efficiently converts CO_2 into CO. Furthermore, a new adsorption-enhanced in-situ-assembled porous structure has been discovered and proved to obtain ~95% surface vacancy oxygen content and various hydrogen evolution sites. Eventually, the yields and volume fractions of H_2 are 11.31 mmol/g and 65.79%, respectively, and the purity of syngas (H_2+CO) reaches 91.82%, which verify its excellent performance in hydrogen reforming and CO_2 conversion.

1. Introduction

Agricultural and forestry practices produce a large amount of biomass waste, and its global annual generation has reached 140 billion tons [1]. Biomass waste, which contains stored chemical energy from the sun, is a kind of renewable energy and is considered as one of substitutes for fossil energy [2]. Due to its excessive accumulation, most governments choose to incinerate biomass waste on-site [3] or send it to municipal landfills [4], which not only waste biomass resources, but also significantly increase greenhouse gas emissions. With the advantages of reductions, harmlessness and high product value, pyrolysis has been demonstrated as a promising path for the recycling of biomass waste [5]. Pyrolysis can convert biomass into coke, oil and synthesis gas, reversing the resource properties of biomass waste, and is an important field of sustainable development.

Several studies have made important contributions to the development of biomass pyrolysis. Direct pyrolysis of biomass at 400–600 ℃ will generate a large amount of tar, which is difficult to separate and purify due to its complex composition [6]. Currently, most researchers use the reforming effect of catalysts to convert tar into H_2-rich syngas at higher temperatures. With high activity and carbon deposition resistance, noble metals, such as Rh, Pt, Pd and Ru, have significant advantages in tar reforming efficiency and the yield of gas and coke [7–9]. However, the high price and low reserves restrict its industrial application. In the non-precious metal catalysts, the cheap transition metals have similar activities to noble metals and are considered to be good substitutes for the latter [10]. The earth-abundant nickel has attracted much attention due to its relatively complete industrial supply chain, but it easily induces carbon deposition on the catalyst surface, resulting in catalytic deactivation and blockage of the reactor [11–13]. Cobalt is another widely used transition metal catalyst with nickel-like activity in catalytic reforming, but the effect of carbon deposition still exists [14–16]. Adding alkali metals or alkaline earth metals is one of the effective methods to improve the coking resistance and catalytic stability of cobalt-based catalysts [17]. Souza et al. show that doping with a small amount of alkali metals (such as Ca, La, Li or Mg) can alter the reduction of cobalt-based catalysts, and improve the catalytic performance and anti-coking performance by changing the acid-base properties. More importantly, they also find that due to the stronger alkaline sites, the Li-modified cobalt catalyst has the lowest coke deposition, which indicates that the gain effect of lithium is the best [18]. However, lithium is very expensive, and it is not economical to directly add lithium to modify the catalysts. Therefore, it is very promising to find a material or waste coexisting with lithium and cobalt as catalyst to

* Correspondence to: School of Environment, Tsinghua University, Room 804, Sino-Italian Environmental and Energy-efficient Building, Beijing 100084, China.
E-mail address: jinhui@tsinghua.edu.cn (J. Li).

https://doi.org/10.1016/j.apcatb.2021.120920
Received 15 July 2021; Received in revised form 2 November 2021; Accepted 9 November 2021
Available online 18 November 2021

co-pyrolyze with biomass waste to reform hydrogen production.

Thanks to the advancement of lithium-ion chemistry technology, lithium-ion batteries (LIBs) have entered our lives in an all-round way, bringing great convenience to human mankind, and won the Nobel Prize in Chemistry in 2019 [19–21]. However, the limitation of cycle life will lead to about 500,000 tons of spent LIBs entering the waste stream every year in China alone [22]. Spent LIBs contain a large amount of heavy metals and toxic electrolytes, so random disposal will seriously threaten ecological safety and human health [23,24]. On the contrary, the high concentration of transition metals promotes spent LIBs to be the urban mines with the most recycling potential [25]. The typical cathode material of spent LIBs is $LiCoO_2$, a layered lithium cobalt metal oxide, which has been reported to have significant catalytic effects on hydrogen production by hydrolysis [26] and degradation of o-phenylphenol [27]. Due to its natural lithium-cobalt intercalation structure, Chen et al. find that the pure $LiCoO_2$ cathode materials in spent LIBs also have a good catalytic effect in the reforming field of biomass pyrolysis gas [28,29]. Furthermore, they also give the detailed mechanism of catalyzing the degradation of lignin and cellulose in sawdust to produce hydrogen when spent LIBs cathode is used as catalyst, as shown in Supplementary Fig. 1 [28]. In addition, Guo et al. suggest that waste $LiCoO_2$ cathodes may have a better catalytic effect due to its the vacancy generation and electronic structure modulation during the continues charging and discharging process [27]. However, the thermal stability of $LiCoO_2$ is poor, and it is prone to structural collapse and lithium volatilization at 800 °C, resulting in catalyst failure. Therefore, how to fix volatile lithium at high temperatures to assist cobalt-based catalysts to reform hydrogen production is a key scientific issue.

Aluminum (Al) foil is a universal carrier of cathode powder, and thus, it is one of the typical materials inherent in spent LIBs. Al foil is a zero-valent aluminum strip, and it may have better reaction potential than zero-valent iron, because it can react with acid and alkali, and has high reducibility. Our previous studies showed that the optimal amount of intrinsic Al foils for in-situ reduction of waste cathode materials could be achieved by mild screening of 4 mm aperture of the crushing products from spent LIBs [30]. Here, we take sawdust as the representative biomass waste, and use the crushing products of cathode strip from spent LIBs as the catalysts to study the pyrolysis reforming behavior of $LiCoO_2$ catalyst in-situ enhanced by Al foils. In order to explore the mechanism of in-situ conversion and hydrogen production, we create a new characterization system with different detection depths, and finally describe the adsorption and desorption process at the atomic level with the assistance of density functional theory (DFT) calculations. Four detection methods are employed: X-ray diffraction (XRD) with a measuring depth of 20–40 μm; energy-dispersive analysis of X-rays (EDAX) with a measuring depth of 0.1–10 μm; X-ray photoelectron spectroscopy (XPS) with a measuring depth of 5–10 nm; and high-resolution transmission electron microscopy (HR-TEM) with a measuring depth of 0.1–1 nm.

2. Experimental methods

2.1. Materials and pretreatment

Spent $LiCoO_2$ batteries from iPhone 6s were donated from an environmental protection technology company in Beijing. The spent LIBs were first immersed in 5% NaCl solution for full discharge, and then manually disassembled in the fume hood to take out their cathode strips. Next, the cathode strips were crushed in a universal grinder for 1–3 min, and then screened by standard sieves with an aperture of 4 or 0.075 mm. The crushing products under the different screens were the raw materials for pyrolysis. Sawdust was another raw material for pyrolysis, and its proximate and ultimate analysis is provided in Table 1.

2.2. Copyrolysis of sawdust and waste electrode materials

The sawdust and crushing products of spent LIBs with different particle sizes were placed in a pyrolysis reactor and a catalytic reactor of a homemade two-stage pyrolysis furnace, respectively. The pyrolysis equipment and specific data of the pyrolysis process are shown in Supplementary Fig. 2. It should be noted here that different crushing products have been used as catalysts for many pyrolysis cycles to detect the performance and stability of the catalyst. When the −0.075 mm crushing products was employed as a catalyst, the results of the first three pyrolysis processes were all poor, so only the first pyrolysis result was analyzed; in contrast, when the −4 mm crushing products was employed as the catalyst for five pyrolysis cycles, the second pyrolysis achieved the best effect, so it could be inferred that the reduction product of the first pyrolysis was the active catalyst structure. After pyrolysis, the solid products from spent LIBs were directly removed from the catalytic reactor, and recycled by grinding dissociation and other sorting methods.

Table 1
Proximate and ultimate analysis of the sawdust.

Proximate analysis (wt% dry basis)	
Moisture	6.66
Volatile matter	74.58
Ash	2.14
Fixed carbon	16.62
Ultimate analysis(wt% dry basis)	
C	46.28
H	6.32
O	46.24
N	1.16

2.3. Material characterization

The phase analysis of the samples was characterized by X-ray diffraction (XRD, Philips PW 1700, USA) using a Cu Kα radiation source (λ = 0.154 nm) with a voltage of 30 kV and a current of 30 mA. The surface morphology, element distribution and elemental content of the samples were characterized by field-emission scanning electron microscopy, equipped with energy dispersive spectroscopy (FESEM and EDS, Carl Zeiss MERLIN Compact, Germany). X-ray photoelectron spectroscopy (XPS, ULVAC-PHI, Inc., Japan) was performed to detect the surface chemical composition of samples using a PHI Quantera SXM instrument. X-ray absorption spectra (XAS) including X-ray absorption near-edge structure (XANES) of the catalysts at Co K-edge / Li K-edge were supported by the Singapore Synchrotron Light Source (SSLS) center. The microcrystalline structures of the samples were analyzed by high resolution transmission electron microscopy (HRTEM, JEOL JEM-2100 F, Japan). The metal element contents in solution were measured by inductively coupled plasma-optical emission spectrometry (ICP-OES, PerkinElmer, OPTIMA 2000, USA).

2.4. Density functional theory calculations

The formation energy and hydrogen evolution mechanism of the pyrolysis products from spent LIBs were calculated by the VASP program software package, which was based on spin-polarized density functional theory (DFT) [31,32]. Furthermore, the projection augmented wave (PAW) method and generalized gradient approximation were adopted, and password based encryption was selected as the exchange correlation function [33,34]. In the calculation, the electron truncation energy was set at 400 eV, and the Monkhorst-Pack k point sampling method was adopted in the Brillouin zone [35]. The convergence standards of the energy and force were set at 10^{-5} eV/atom and 0.01 eV/Å, respectively.

2.5. Calculation of the gas quality from pyrolysis

In this study, gas chromatography (Micro GC, 3000, Inficon, Switzerland) was employed to provide the partial pressure of each

component (H_2, CH_4, CO_2 and CO) in the pyrolysis gas every 2 min. Assuming that the entire pyrolysis process lasts 2n minutes, the pyrolysis yield of a certain gas component per unit of (φ, mmoL/g) is calculated as follows:

$$\varphi = \frac{\sum_{m=1}^{n} (L_m * V_m * 2)}{C * M} \quad (12)$$

where L_m is the working condition flow at the 2 m min, mL/min; V_m is the partial pressure of a certain gas component at the 2 m min, %; C is the standard molar volume of the gas, namely, 22.4 L/mol; M is the mass consumed by pyrolysis, g. Furthermore, the volume fraction of H_2 (β, %) can be calculated as follows:

$$\beta = \frac{\varphi_{H_2}}{\varphi_{H_2} + \varphi_{CH_4} + \varphi_{CO_2} + \varphi_{CO}} * 100\% \quad (13)$$

3. Results and discussion

3.1. Excellent catalytic reforming effects: efficient H_2 production and CO_2 suppression

The gas distribution in Fig. 1 and the detailed data in Supplementary Fig. 3–18 show that the yield and volume fraction of H_2 without a catalyst are 3.85 mmol/g and 21.20%, respectively, and the volume fraction of synthetic gas composed of H_2 and CO is only 52.29%, so the effect of hydrogen production by direct pyrolysis is poor. When −0.075 mm crushing cathode materials from spent LIBs are employed as a catalyst, the volume fraction of H_2 increases by 10%, and the CO_2 content sharply decreases to 1/10 of that without any catalyst; however, the hydrogen production is still unsatisfactory. When −4 mm crushing cathode materials from spent LIBs are selected as the catalyst, the highest yield and volume fraction of H_2 increase to 11.31 mmol/g and 65.79%, respectively, and the volume fraction of synthetic gas increases to 91.82%, showing a significant catalytic effect. It should be noted that the optimal H_2 yield in water electrolysis is 20 μmol/min and 1.2 mmol hydrogen can be produced in one hour, which is only one tenth of the hydrogen production efficiency of this study [36]. On the other hand, the volume fraction of CO_2 here is only 1.72%, and the volume ratio of H_2/CO_2 is 38.25, which is 8 times of that in methane steam reforming [37]. Therefore, the actual effect of pyrolysis and reforming of sawdust with −4 mm crushing cathode materials as catalyst has been better than methane steam reforming and water electrolysis to some extent. Although cobalt-based materials can promote the hydrogen evolution reaction, there is no indication that the crushing cathode materials from spent LIBs can strongly enhance the hydrogen production during pyrolysis while simultaneously providing a satisfactory CO_2 suppression effect [38]. Therefore, it is necessary to systematically analyze the catalytic reforming behavior of the crushing products with different particle sizes from spent LIBs to reveal the in-situ enhanced mechanism of Li-Co catalysts.

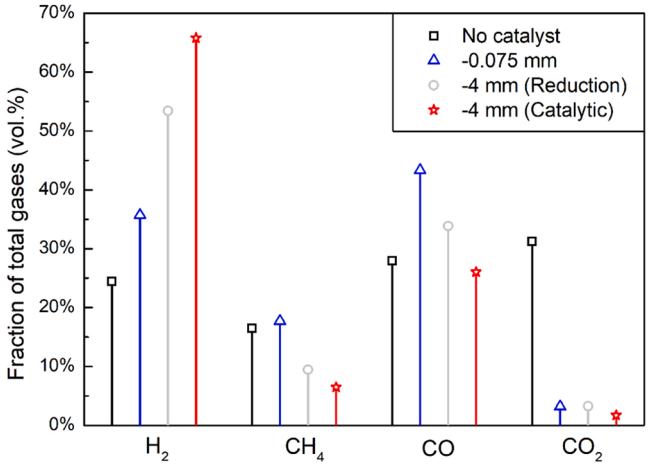

Fig. 1. Gas distribution of sawdust pyrolysis with different catalysts from spent lithium-ion batteries.

3.2. Phase composition and morphological evidence: Co nanoflowers and $LiAlO_2$@CoO nanoporous network

First of all, due to the good ductility of Al foils, the crushing of the cathode electrode from spent LIBs exhibits a good selective crushing behavior, that is, the crushed Al foils product has a large particle size, while the crushed $LiCoO_2$ product has a small particle size. More importantly, the 0.075-mm sieve separation can completely sieve out the Al foil, so −0.075 mm crushing product is only $LiCoO_2$, while −4 mm crushing product is a mixture of $LiCoO_2$ and Al foils, as shown in Fig. 2A. XRD analysis of pyrolysis products in Fig. 2B give that when $LiCoO_2$ powder is employed as catalyst, the catalytic product is only Co, which indicates the volatilization of lithium at a high temperature; in contrast, when a mixture of $LiCoO_2$ and Al foils is used for co-pyrolysis with sawdust, they will first react to form a catalyst composed of $LiAlO_2$, CoO and Co, and the final pyrolysis products are $LiAlO_2$ and Co. It suggests that by introducing aluminum foil, we successfully fix and recover light Li atoms at 800 ℃. Combined with previous composition analysis of pyrolysis gas, it can be found that the new catalyst prepared by the pyrolysis of $LiCoO_2$ and Al exhibits observably good effects on hydrogen evolution, while the traditional Co catalyst prepared by the pyrolysis of $LiCoO_2$ demonstrates a poor effect, which is very necessary to conduct in-depth analysis and discussion.

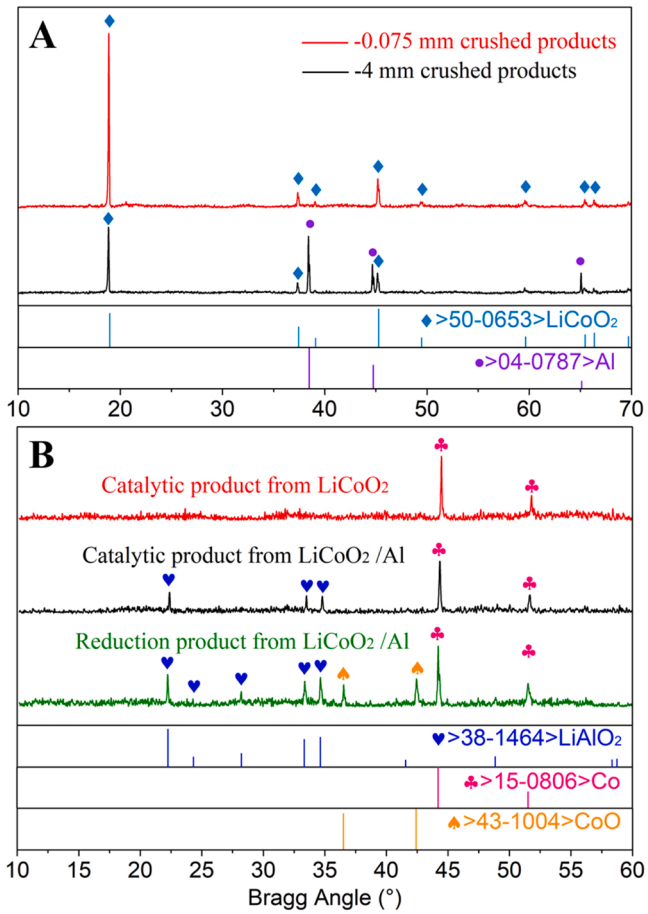

Fig. 2. XRD phase analysis of raw materials (A) and pyrolysis products (B).

The surface morphology in Fig. 3 shows that the $LiCoO_2$ in spent LIBs is a massive micron-sized particle with a smooth surface, as shown in Fig. 3A, while its pyrolysis product (pure Co) is an agglomeration of small particles, as shown in Fig. 3B. In view of the similar morphology and size of $LiCoO_2$ particles and single Co particle, it can be inferred that the decomposition reaction of $LiCoO_2$ occurs in the reducing gases generated by sawdust pyrolysis, resulting in the generation of Li_2CO_3 and Co. The possible reaction Eqs. (1–6) are as follows. However, the melting point of Li_2CO_3 is lower than 750 °C and volatilization loss occurs during pyrolysis at 800 °C, so only agglomerated Co particles are left [39].

$$2LiCoO_2 + CO_2 \xrightarrow{\Delta} Li_2CO_3 + Co_2O_3 \quad (1)$$

$$2LiCoO_2 + CO \xrightarrow{\Delta} Li_2CO_3 + 2CoO \quad (2)$$

$$Co_2O_3 + CO \xrightarrow{\Delta} CO_2 + 2CoO \quad (3)$$

$$Co_2O_3 + H_2 \xrightarrow{\Delta} H_2O + 2CoO \quad (4)$$

$$CoO + CO \xrightarrow{\Delta} CO_2 + Co \quad (5)$$

$$CoO + H_2 \xrightarrow{\Delta} H_2O + Co \quad (6)$$

In Fig. 3C–I, the high-efficiency catalyst prepared from $LiCoO_2$ and Al in spent LIBs has a unique morphology and structure; the substrate is reported to be an advanced porous structure, as shown in Supplementary Fig. 19, while its core consists of Co nanoflowers [40]. Interestingly, a small amount of a similar porous structure also appears on the surface of the pyrolysis product of $LiCoO_2$, as shown in Supplementary Fig. 20, and its elemental analysis suggests that this is CoO. The further element

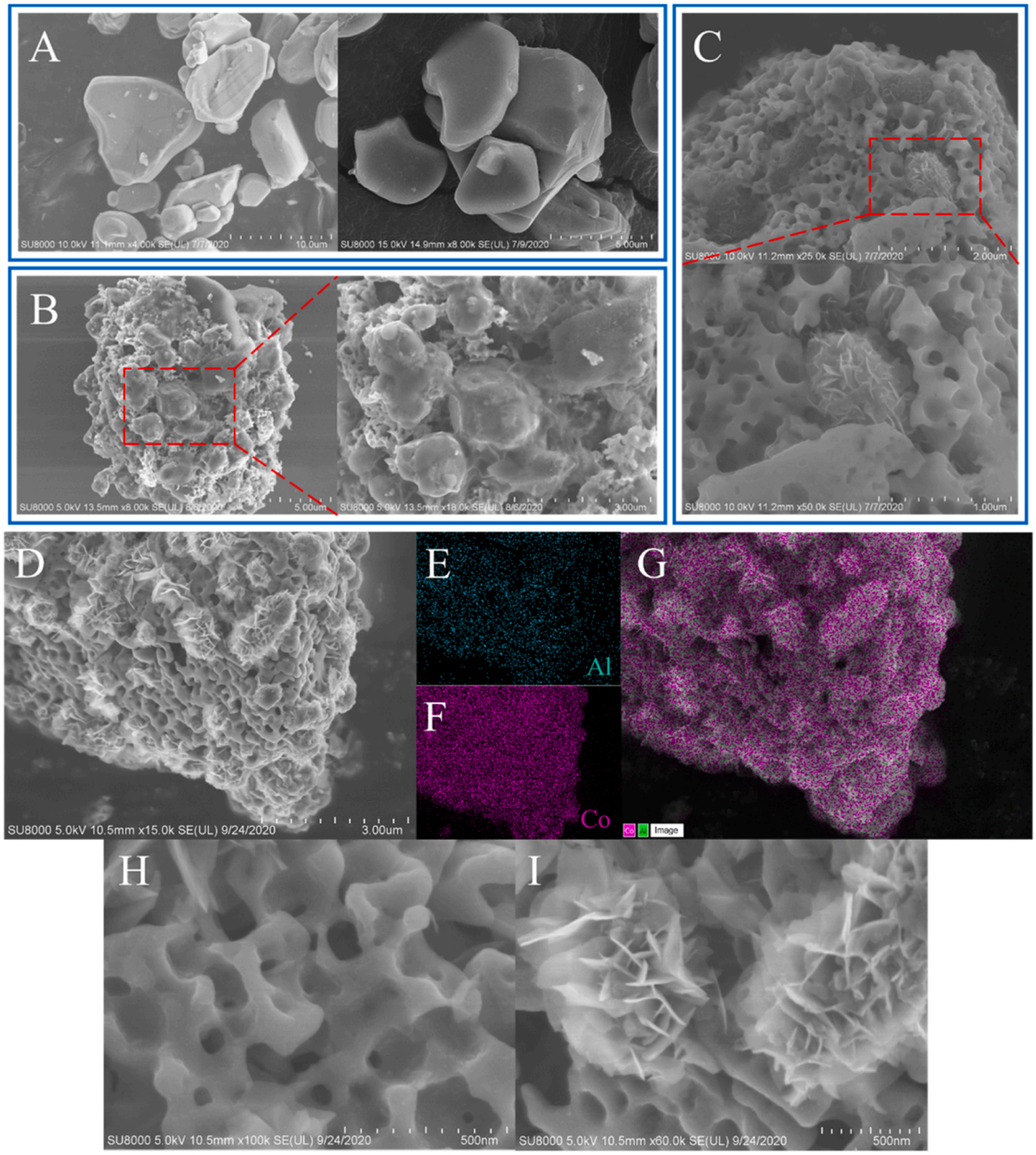

Fig. 3. Micromorphology and elemental distributions of different pyrolysis products, A the crushed products of cathode materials in spent LIBs; B. the pyrolysis products of $LiCoO_2$ from spent LIBs; C and D. the pyrolysis products of $LiCoO_2$ and Al from spent LIBs; E. elemental distribution of Al; F. elemental distribution of Co; G. elemental distribution of Co and Al; H. the local nanoporous network in D; I. the Co nanoflowers in D).

distributions in Fig. 3E–G show that the uniform doping of Al promotes the stable existence of the porous structure and connects to form a nanoporous network, as shown in Fig. 3H. Combined with an XRD phase analysis in Fig. 2B, it is considered that the nanoporous network is formed by CoO doped with $LiAlO_2$. This Co nanoflower and $LiAlO_2$@-CoO nanoporous network structure, as shown in Fig. 3I may be generated by the following displacement reaction (7).

$$LiCoO_2 + Al \xrightarrow{\Delta} LiAlO_2 + Co \quad (7)$$

Under the guidance of displacement reaction, part of Co atoms in the waste cathodes protrude out of the body of $LiCoO_2$ particles and grow into perfect Co nanoflowers, which likely increases surface activity. Additionally, part of Al atoms are pulled into the $LiCoO_2$ particles to replace the Co atoms, thereby forming $LiAlO_2$ with a lower crystal energy (proven by subsequent DFT calculations). The replacement path or channel of Co and Al atoms, entering and exiting the $LiCoO_2$ particles, may be the main reason for the formation of the porous network structure. It should be noted that this replacement reaction will first occur on the surface of the $LiCoO_2$ particles, and then slowly extend to the inside of the particles, while the original $LiCoO_2$ inside the particles will also degrade to form CoO at the initial stage of pyrolysis. It is the external replacement reaction and internal degradation process that together result in the in-situ-assembled formation of Co nanoflowers and $LiAlO_2$@CoO nanoporous network.

3.3. Catalytic performance exploration: surface activity and hydrogen evolution sites

XPS technology can analyze the functional group structure at depths of 5–10 nm on the material surface, and this technique is employed to compare the surface composition of the new in-situ-assembled catalyst and a traditional Co catalyst. XAS technology can reveal the chemical environment around atoms and is used to characterize the valence states

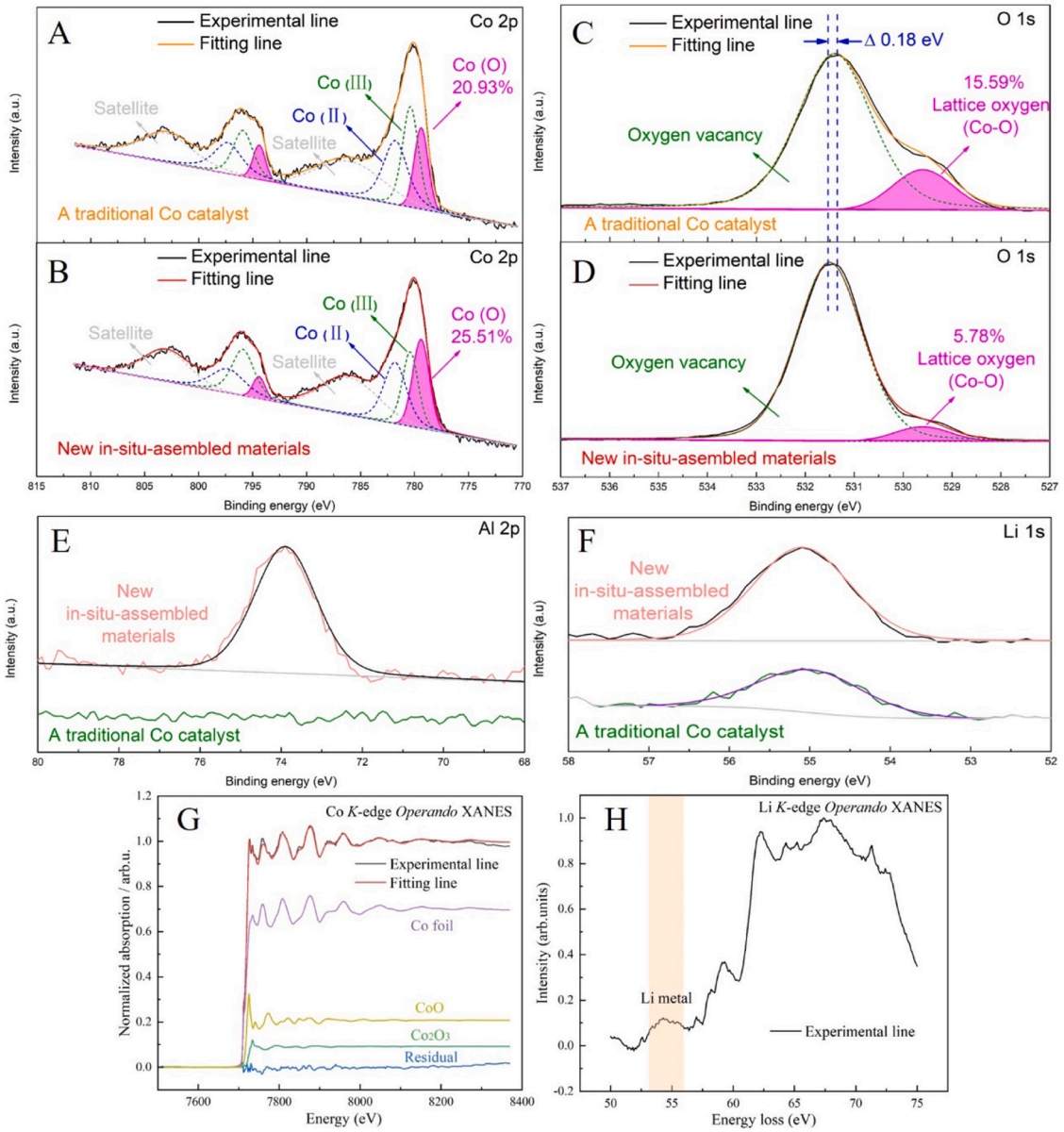

Fig. 4. Surface compositions and activity analysis of different pyrolysis products, A and B. the Co 2p XPS spectra, where 779.4 eV and 794.4 eV are the characteristic peaks of Co^0, 780.4 eV and 795.9 eV are the characteristic peaks of Co^{3+}, 781.8 eV and 797.3 eV are the characteristic peaks of Co^{2+}; C. the Al 2p XPS spectra; D and E. the O 1 s XPS spectra, where 529.6 eV is lattice oxygen and 531.4 eV is oxygen vacancy; F. the Li 1s XPS spectra; G. the Co K-edge XANES of new in-situ-assembled materials; H. the Li K-edge XANES of new in-situ-assembled materials) [20,38].

of key atoms. The Co 2p XPS spectra in Figs. 4A and B show that there are more zero-valent Co (25.51%) on the surface of the in-situ-assembled catalyst generated from $LiCoO_2$ and Al, compared with the traditional catalyst prepared from $LiCoO_2$. The Co k-edge XANES spectrum in Fig. 4G gives that there are 64% zero-valent Co, 26% divalent Co and 10% trivalent Co in the new in-situ-assembled catalyst. The higher content of zero-valent Co proves that the in-situ-assembled catalyst has better reforming performance [41–43]. On the other hand, the O 1 s XPS spectra in Figs. 4C and D show that there are more oxygen vacancies on the surface of the in-situ-assembled catalyst. Surface oxygen vacancies can promote hydrocarbon reforming by lowering the activation barriers for forming of CH_3, CH_2 and CH species [21,44]. The oxygen vacancy content of the in-situ-assembled catalyst is as high as 94.22% at 531.4 eV, which is a typical defect-rich oxide with better catalytic potential. The Al 2p and Li 1s XPS spectra in Figs. 4E and F show that both the Al and Li fitting curves of the in-situ-assembled catalyst have obvious bulges, proving that $LiAlO_2$ is attached to the catalyst surface. More importantly, at 55 eV in the Li K-edge XANES spectrum in Fig. 4H is a characteristic peak of Li metal [45]. This is the zero-valent lithium formed by Li^+ in the structure of $LiCoO_2$ or $LiAlO_2$ moving to the surface of the catalysts to obtain electrons, which implies the existence of electrochemical reactions during the catalytic process.

The microcrystalline structure analysis based on HRTEM in Supplementary Fig. 21 further proves that the porous structure of the in-situ-assembled catalyst is attached with a $LiAlO_2$ layer, and its (102) crystal plane is exposed to the outside. As the skeleton of porous structure, CoO is hidden in the interior of this porous structure, while the core part is Co particle with its (111) crystal plane exposed. Therefore, it can be concluded that the excellent catalytic performance of the in-situ-assembled catalyst mainly comes from the (111) crystal plane of the Co nanoflowers and the (102) crystal plane of $LiAlO_2$ on the surface of the nanoporous network.

Generally, hydrogen production includes four steps, namely, proton adsorption, reduction on the catalyst surface to form H^+, H_2 formation and desorption [46]. Accordingly, the Gibbs free energy (ΔG_H) can be calculated by DFT to estimate the hydrogen evolution reaction activity of the (111) crystal plane of Co and the (102) crystal plane of $LiAlO_2$, as shown in Fig. 5. $LiAlO_2$ has an olivine structure, as shown in Fig. 5A, and B provides possible hydrogen absorption sites on the (102) crystal plane, including sites 1 and 4 for Al atoms and sites 2 and 3 for O atoms, and their adsorption behaviors with the white spheres of H atoms are shown in Fig. 5C–F in turn. The hydrogen absorption and evolution capacity of each active site on the (102) crystal plane of $LiAlO_2$ in Fig. 5M shows that only the oxygen adsorption site at site 3 can promote the hydrogen evolution reaction to proceed spontaneously due to its $\Delta G_H \leq 0$. This is because in the $LiAlO_2$ structure, each Al atom is bonded with the three oxygen atoms, which are in the saturated state; thus, there is no additional hydrogen absorption site, resulting in weak hydrogen evolution capacity. Furthermore, each oxygen atom is only bonded with one Al atom, and there is an extra electron around it, so it is easy to bond with a hydrogen atom to form a hydrogen bond, thereby showing good hydrogen absorption performance. In particular, the oxygen atom at site 2 is attracted by the Al atom inside the crystal structure and is in a concave position on the surface. If a hydrogen bond is formed, it requires a longer bond length, so it is difficult for the O at site 2 to adsorb a H atom.

The unit cell of cobalt is a face-centered structure, as shown in Fig. 5G. There are many electrons in the outer layer of transition metal Co, which is theoretically easy to adsorb hydrogen atoms. However, due to the different distances from internal Co atoms to the surface, they can

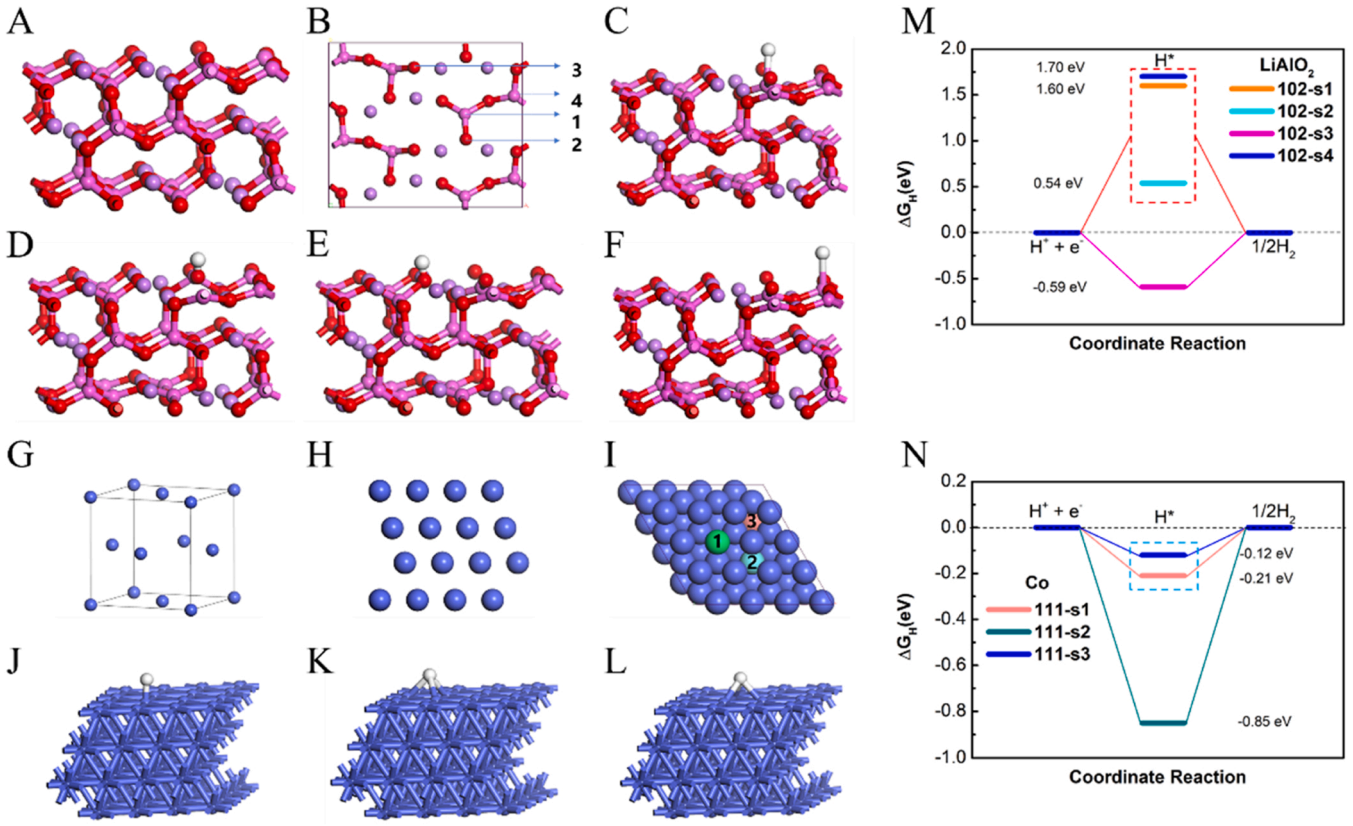

Fig. 5. Catalytic effects of cobalt and $LiAlO_2$ for hydrogen evolution reaction based on density functional theory, A the front view of (102) crystal plane in $LiAlO_2$; B. the top view of (102) crystal plane in $LiAlO_2$; C–F. hydrogen evolution sites on the surface of (102) crystal plane in $LiAlO_2$; G. crystal cell structure of Co; H. the front view of (111) crystal plane in Co; I. the top view of (111) crystal plane in Co; J–L. hydrogen evolution sites on the surface of (111) crystal plane in Co; M and N. the hydrogen absorption and evolution capacity of each active site on the (102) crystal plane of $LiAlO_2$ and the (111) crystal plane in Co, respectively).

be divided into three kinds of Co adsorption sites, as shown in Fig. 5I, and their adsorption behaviors are shown in Fig. 5J–L. The DFT results in Fig. 5N show that all three hydrogen absorption sites can spontaneously adsorb hydrogen, reform and produce H_2. It should be noted that the absolute value of ΔG_H at site 2 of Co is notably large (the best value is 0 eV). This means that the hydrogen adsorption at this point site will be too stable to desorb, which also leads to poor hydrogen production [47]. Therefore, both the Co nanoflowers and nanoporous network of the in-situ-assembled catalyst can promote the hydrogen evolution reaction. Since the order of catalytic activity of the hydrogen absorption sites on the exposed crystal plane is Co s3 > Co s1 > $LiAlO_2$ s3, the Co nanoflower is the key active material for reforming and H_2 production.

3.4. Mechanism model of catalytic reforming behavior of Li-Co catalyst in-situ enhanced by Al foils in spent lithium ion batteries

$LiCoO_2$ cathode in spent LIBs is a kind of lamellar crystal, and its stable layered structure provides a fast channel for the insertion and deintercalation of lithium ions (Li^+), as shown in Fig. 6A. $LiAlO_2$ is an ionic crystal with an olivine structure composed of tetrahedral unit cells, consisting of Al and O atoms, as shown in Fig. 6B. Although Li^+ can still shuttle between $LiAlO_2$ crystals to a certain extent, it has formed a similar crystal cage structure, which protects Li^+ from volatilization at high temperatures. According to the phase analysis in Fig. 2, the morphological observation in Fig. 3, and the crystal distribution in Supplementary Fig. 21, we have determined that the displacement reaction between $LiCoO_2$ particles and Al foils would occur during the co-pyrolysis of sawdust to produce Co and $LiAlO_2$. Furthermore, the intermediates in the pyrolysis process will be actively assembled into a special structure of Co nanoflowers and $LiAlO_2$ @CoO nanoporous network, which is made of CoO skeleton and $LiAlO_2$ film layer.

Based on the functional groups of metallic lithium and Li_2CO_3 found on the in-situ-assembled catalyst by XAS in Fig. 4H and XPS in Supplementary Fig. 22, it can be inferred that the Li^+ in the $LiAlO_2$ crystals may react with the CO_2 generated by sawdust pyrolysis to form a similar Li-CO_2 battery system [48], as shown in Fig. 6C. The specific reaction equations are shown as follows:

$$\text{Cathodic: } 4Li^+ + 3CO_2 + 4e^- \rightarrow 2Li_2CO_3 + C,\ U = 2.8\text{V versus Li/Li}^+ \quad (8)$$

$$\text{Anodic: } 2Li_2CO_3 \rightarrow 4Li^+ + O_2 + 2CO_2 + 4e^-,\ U = 3.82\text{V versus Li/Li}^+ \quad (9)$$

$$\text{Overall reaction: } 3CO_2 \rightarrow 2CO_2 + C + O_2 \quad (10)$$

This galvanic interaction can decompose CO_2 into C and O_2, and then the carbon will react with CO_2 to produce CO at a high temperature. The specific reaction is as follows:

$$C + CO_2 \xrightarrow{\Delta} 2CO \quad (11)$$

It should be noted that sawdust pyrolysis will produce a steady stream of CO_2. Thus, reaction (11) will not decrease the partial pressure of CO_2 in the reactor but will promote the forward progress of galvanic reaction (10) by decomposing the newly formed C, which will further accelerate the decomposition of CO_2. When all the CO_2 has been reacted, Li^+ will absorb the remaining electrons to generate metallic lithium on the catalyst surface. This mechanism fully explains the CO_2 suppression or CO_2 degradation process when $LiCoO_2$ and $LiAlO_2$ are used as catalysts. Therefore, from the trace lithium metal and Li_2CO_3 on the surface, we infer the possibility of the Li-CO_2 galvanic cell reaction, and predict that this will greatly promote the degradation of CO_2 in the pyrolysis gas.

The SEM and EDAX analysis in Fig. 3 and Supplementary Fig. 23 show that the $LiAlO_2$@CoO nanoporous network, formed by doping ~2% $LiAlO_2$ into CoO, firmly fixes the Co nanoflowers and disperses them one by one, effectively avoiding their agglomeration and improving their catalytic activity and stability, as shown in Fig. 6D. On the other hand, the crystal lattice analysis of HRTEM in Supplementary Fig. 21 shows that $LiAlO_2$, attached to the surface of the nanoporous network, exposes the (102) crystal planes, which has been proven by DFT calculations in Fig. 5 that approximately 1/2 of the oxygen sites in the structure have good catalytic effects on the hydrogen evolution reaction, as shown in Fig. 6E. In particular, the Li-CO_2 galvanic battery system may generate a potential of approximately 2.8 V, which may excite all 4 hydrogen evolution sites on the surface of the (102) plane of $LiAlO_2$. Although the hydrogen evolution ability of Co nanoflower is

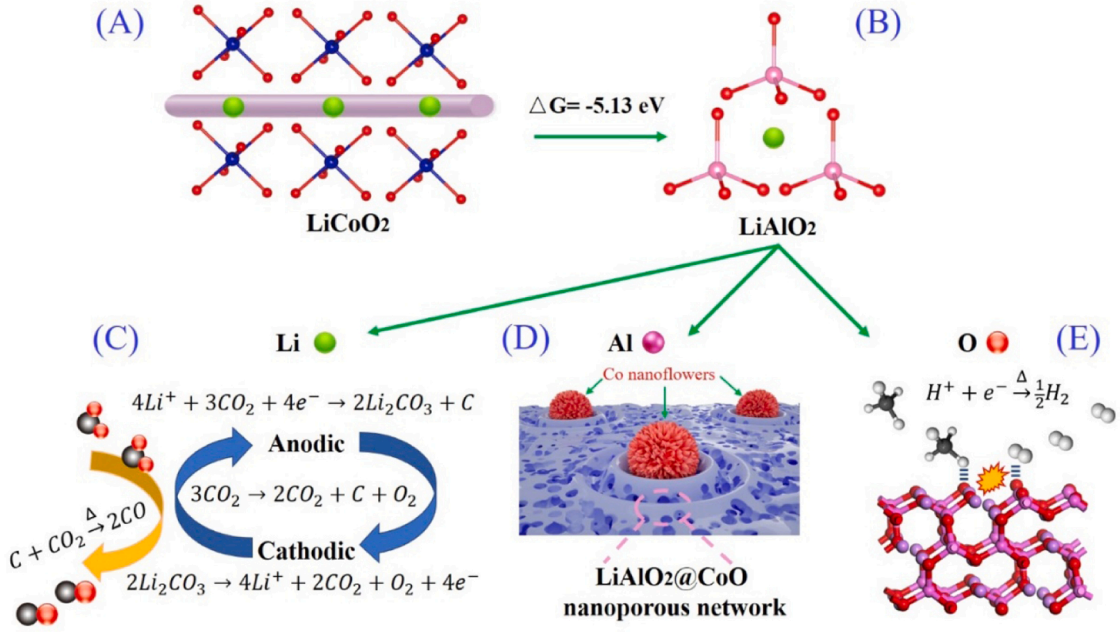

Fig. 6. Pyrolysis catalytic mechanism of sorption-enhanced in-situ-assembled porous structure, A.fast transmission channel of Li^+ in $LiCoO_2$; B. crystal cage of Li^+ in $LiAlO_2$; C. possible CO_2 degradation process by Li-CO_2 battery system; D. Co nanoflowers and $LiAlO_2$@CoO nanoporous network; E. hydrogen evolution on the surface of $LiAlO_2$).

stronger, the $LiAlO_2$@CoO nanoporous network mainly plays a role at the pre-adsorption stage of the pyrolysis process, attracting hydrocarbons around the catalyst to be reformed by the Co nanoflowers and produce hydrogen. Therefore, by constructing a $LiAlO_2$@CoO nanoporous network, increasing the number of hydrogen evolution sites on the surface and inducing the galvanic reaction, efficient hydrogen production and the selective suppression of CO_2 are achieved at the same time in regard to the physical structure, catalytic activity and surface chemical reaction.

4. Conclusion

With good catalytic activity and carbon deposition resistance, the cathode materials of spent LIBs, as a cheap waste with a natural content of a large amount of cobalt and lithium, is very promising to be used as a catalyst for pyrolysis reforming of biomass waste to produce hydrogen. Although current researches have explained the mechanism of transition metal oxides in spent LIBs to catalyze the pyrolysis reforming of lignin and fibers, the role of lithium is still blank. In this paper, we have first proved that during the direct pyrolysis reforming process of spent $LiCoO_2$ cathode and sawdust, the high-temperature volatilization of lithium would cause the crystal lattice of $LiCoO_2$ to collapse and degrade into agglomerated Co particles, thereby losing catalytic activity. In order to fix alkali metal lithium at 800 ℃ to optimize the catalytic performance of Co-based catalyst, we successfully convert $LiCoO_2$ into $LiAlO_2$ with a higher melting point by introducing Al foils inherent in spent LIBs. More importantly, driven by the displacement reaction, a sorption-enhanced in-situ-assembled catalytic structure, Co nanoflowers and $LiAlO_2$@CoO nanoporous network, can be formed with ~95% oxygen vacancy content, various hydrogen evolution sites and a similar Li-CO_2 battery system. It is this novel catalytic structure that contributes to the excellent hydrogen production, that is, the yields and volume fractions of H_2 are 11.31 mmol/g and 65.79%, respectively, and the volume fraction of synthetic gas reaches 91.82%, which is the first time that the purity of synthetic gas prepared by Co-based catalytic materials is increased to 90%. Furthermore, this in-situ-assembled catalytic structure will eventually be degraded into Co and $LiAlO_2$, which can be easily recycled by sorting methods, avoiding heavy metal pollution from spent catalysts.

CRediT authorship contribution statement

Jiadong Yu: Writing – original draft, Writing – review & editing, Conceptualization, Methodology, Visualization. **Shujuan Zou:** Resources, Experimental design, Experimenter. **Guiyin Xu:** Formal analysis, Project administration. **Lili Liu:** Resources, Supervision, Project administration. **Ming Zhao:** Data curation, Resources. **Jinhui Li:** Software, Conceptualization, Supervision, Project administration, Funding acquisition.

Declaration of Competing Interest

The authors declare that they have no known competing financial interests or personal relationships that could have appeared to influence the work reported in this paper.

Acknowledgments

This research is supported by financial supports by National Natural Science Foundation of China (71804085).

Appendix A. Supporting information

Supplementary data associated with this article can be found in the online version at doi:10.1016/j.apcatb.2021.120920.

References

[1] N. Tripathi, C.D. Hills, R.S. Singh, C.J. Atkinson, Biomass waste utilisation in low-carbon products: harnessing a major potential resource, NPJ Clim. Atmos. Sci. 2 (2019).
[2] L. Gustavsson, P. Svenningsson, Substituting fossil fuels with biomass, Energy Convers. Manag. 37 (1996) 1211–1216.
[3] R. Gumisiriza, J.F. Hawumba, M. Okure, O. Hensel, Biomass waste-to-energy valorisation technologies: a review case for banana processing in Uganda, Biotechnol. Biofuels 10 (2017).
[4] L. Matsakas, Q. Gao, S. Jansson, U. Rova, P. Christakopoulos, Green conversion of municipal solid wastes into fuels and chemicals, Electron. J. Biotechnol. 26 (2017) 69–83.
[5] X. Hu, M. Gholizadeh, Biomass pyrolysis: a review of the process development and challenges from initial researches up to the commercialisation stage, J. Energy Chem. 39 (2019) 109–143.
[6] D. Mohan, C.U. Pittman, P.H. Steele, Pyrolysis of wood/biomass for bio-oil: a critical review, Energy Fuels 20 (2006) 848–889.
[7] K. Tomishige, T. Miyazawa, M. Asadullah, S. Ito, K. Kunimori, Catalyst performance in reforming of tar derived from biomass over noble metal catalysts, Green Chem. 5 (2003) 399–403.
[8] J.H. Chen, M. Tamura, Y. Nakagawa, K. Okumura, K. Tomishige, Promoting effect of trace Pd on hydrotalcite-derived Ni/Mg/Al catalyst in oxidative steam reforming of biomass tar, Appl. Catal. B Environ. 179 (2015) 412–421.
[9] N. Kopfle, T. Gotsch, M. Grunbacher, E.A. Carbonio, M. Havecker, A. Knop-Gericke, L. Schlicker, A. Doran, D. Kober, A. Gurlo, S. Penner, B. Klotzer, Zirconium-assisted activation of palladium to boost syngas production by methane dry reforming, Angew. Chem. Int. Ed. 57 (2018) 14613–14618.
[10] B. Abdullah, N.A.A. Ghani, D.V.N. Vo, Recent advances in dry reforming of methane over Ni-based catalysts, J. Clean. Prod. 162 (2017) 170–185.
[11] Z.Y. Hou, T. Yashima, Supported Co catalysts for methane reforming with CO_2, React. Kinet. Catal. Lett. 81 (2004) 153–159.
[12] L.P.R. Profeti, E.A. Ticianelli, E.M. Assaf, Co/Al_2O_3 catalysts promoted with noble metals for production of hydrogen by methane steam reforming, Fuel 87 (2008) 2076–2081.
[13] M. Wolf, Thermodynamic assessment of the stability of bulk and nanoparticulate cobalt and nickel during dry and steam reforming of methane, RSC Adv. 11 (2021) 18187–18197.
[14] N. Logeshwaran, S. Ramakrishnan, S.S. Chandrasekaran, M. Vinothkannan, A. R. Kim, S. Sengodan, D.B. Velusamy, P. Varadhan, J.H. He, D.J. Yoo, An efficient and durable trifunctional electrocatalyst for zinc-air batteries driven overall water splitting, Appl. Catal. B Environ. 297 (2021).
[15] S. Ramakrishnan, J. Balamurugan, M. Vinothkannan, A.R. Kim, S. Sengodan, D. J. Yoo, Nitrogen-doped graphene encapsulated FeCoMoS nanoparticles as advanced trifunctional catalyst for water splitting devices and zinc-air batteries, Appl. Catal. B Environ. 279 (2020).
[16] E. Vijayakumar, S. Ramakrishnan, C. Sathiskumar, D.J. Yoo, J. Balamurugan, H. S. Noh, D. Kwon, Y.H. Kim, H. Lee, MOF-derived CoP-nitrogen-doped carbon@ NiFeP nanoflakes as an efficient and durable electrocatalyst with multiple catalytically active sites for OER, HER, ORR and rechargeable zinc-air batteries, Chem. Eng. J. 428 (2022), 131115.
[17] K. Takanabe, K. Nagaoka, K. Nariai, K. Aika, Influence of reduction temperature on the catalytic behavior of Co/TiO_2 catalysts for CH_4/CO_2 reforming and its relation with titania bulk crystal structure, J. Catal. 230 (2005) 75–85.
[18] G. de Souza, N.R. Marcilio, O.W. Perez-Lopez, Dry reforming of methane at moderate temperatures over modified Co-Al co-precipitated catalysts, Mater. Res. 17 (2014) 1047–1055.
[19] J.D. Yu, M.S. Lin, Q.Y. Tan, J.H. Li, High-value utilization of graphite electrodes in spent lithium-ion batteries: From 3D waste graphite to 2D graphene oxide, J. Hazard. Mater. 401 (2021).
[20] K. Liu, Q.Y. Tan, L.L. Liu, J.H. Li, Acid-free and selective extraction of lithium from spent lithium iron phosphate batteries via a mechanochemically induced isomorphic substitution, Environ. Sci. Technol. 53 (2019) 9781–9788.
[21] M.M. Wang, Q.Y. Tan, J.H. Li, Unveiling the role and mechanism of mechanochemical activation on lithium cobalt oxide powders from spent lithium-ion batteries, Environ. Sci. Technol. 52 (2018) 13136–13143.
[22] X.L. Zeng, R.Y. Gong, W.Q. Chen, J.H. Li, Uncovering the recycling potential of "New" WEEE in China, Environ. Sci. Technol. 50 (2016) 1347–1358.
[23] J.D. Yu, Y.Q. He, Z.Z. Ge, H. Li, W.N. Xie, S. Wang, A promising physical method for recovery of $LiCoO_2$ and graphite from spent lithium-ion batteries: grinding flotation, Sep. Purif. Technol. 190 (2018) 45–52.
[24] J.D. Yu, Y.Q. He, H. Li, W.N. Xie, T. Zhang, Effect of the secondary product of semi-solid phase Fenton on the flotability of electrode material from spent lithium-ion battery, Powder Technol. 315 (2017) 139–146.
[25] X.L. Zeng, J.A. Mathews, J.H. Li, Urban mining of E-waste is becoming more cost-effective than virgin mining, Environ. Sci. Technol. 52 (2018) 4835–4841.
[26] P. Krishnan, K.L. Hsueh, S.D. Yim, Catalysts for the hydrolysis of aqueous borohydride solutions to produce hydrogen for PEM fuel cells, Appl. Catal. B Environ. 77 (2007) 206–214.
[27] H. Guo, Z.J. Min, Y. Hao, X. Wang, J.C. Fan, P.H. Shi, Y.L. Min, Q.J. Xu, Sustainable recycling of $LiCoO_2$ cathode scrap on the basis of successive peroxymonosulfate activation and recovery of valuable metals, Sci. Total Environ. 759 (2021).
[28] L. Chen, P. Wang, Y.F. Shen, M.M. Guo, Spent lithium-ion battery materials recycling for catalytic pyrolysis or gasification of biomass, Bioresour. Technol. 323 (2021).

[29] P. Wang, L. Chen, Y. Shen, Recycling spent ternary lithium-ion batteries for modification of dolomite used in catalytic biomass pyrolysis – a preliminary study by thermogravimetric and pyrolysis-gas chromatography/mass spectrometry analysis, Bioresour. Technol. 337 (2021).
[30] J.D. Yu, Q.Y. Tan, J.H. Li, Exploring a green route for recycling spent lithium-ion batteries: revealing and solving deep screening problem, J. Clean. Prod. 255 (2020).
[31] S. Kambayashi, J. Chihara, Ab initio molecular dynamics for simple liquid metals based on the hypernetted-chain approximation, Mol. Simul. 16 (1996) 31–46.
[32] G. Kresse, J. Furthmuller, Efficient iterative schemes for ab initio total-energy calculations using a plane-wave basis set, Phys. Rev. B 54 (1996) 11169–11186.
[33] G. Kresse, D. Joubert, From ultrasoft pseudopotentials to the projector augmented-wave method, Phys. Rev. B 59 (1999) 1758–1775.
[34] J.P. Perdew, K. Burke, M. Ernzerhof, Generalized gradient approximation made simple, Phys. Rev. Lett. 77 (1996) 3865–3868.
[35] H.J. Monkhorst, J.D. Pack, Special points for brillouin-zone integrations, Phys. Rev. B 13 (1976) 5188–5192.
[36] X.Y. Lu, Q.R. Zhang, Y.H. Ng, C.A. Zhao, Reversible ternary nickel-cobalt-iron catalysts for intermittent water electrolysis, EcoMat 2 (2020).
[37] S. Akbari-Emadabadi, M.R. Rahimpour, A. Hafizi, P. Keshavarz, Promotion of Ca-Co bifunctional catalyst/sorbent with yttrium for hydrogen production in modified chemical looping steam methane reforming process, Catalysts 7 (2017).
[38] M. Zhao, T.L. Church, A.T. Harris, SBA-15 supported Ni-Co bimetallic catalysts for enhanced hydrogen production during cellulose decomposition, Appl. Catal. B Environ. 101 (2011) 522–530.
[39] W.Q. Wang, Y.C. Zhang, X.G. Liu, S.M. Xu, A simplified process for recovery of Li and Co from spent $LiCoO_2$ cathode using Al foil as the in situ reductant, ACS Sustain. Chem. Eng. 7 (2019) 12222–12230.
[40] H. Wang, X. Wang, M. Li, L. Zheng, D. Guan, X. Huang, J. Xu, J. Yu, Porous materials applied in nonaqueous Li-O_2 batteries: status and perspectives, Adv. Mater. 32 (2020), e2002559.
[41] S. Losse, J.G. Vos, S. Rau, Catalytic hydrogen production at cobalt centres, Coord. Chem. Rev. 254 (2010) 2492–2504.
[42] K. Tang, C.Z. Yuan, Y. Xiong, H.B. Hu, M.Z. Wu, Inverse-opal-structured hybrids of N, S-codoped-carbon-confined Co_9S_8 nanoparticles as bifunctional oxygen electrocatalyst for on-chip all-solid-state rechargeable Zn-air batteries, Appl. Catal. B Environ. 260 (2020).
[43] Z.Q. Cao, M.Z. Wu, H.B. Hu, G.J. Liang, C.Y. Zhi, Monodisperse Co_9S_8 nanoparticles in situ embedded within N, S-codoped honeycomb-structured porous carbon for bifunctional oxygen electrocatalyst in a rechargeable Zn-air battery, NPG Asia Mater. 10 (2018) 670–684.
[44] L. Zeng, Z. Cheng, J.A. Fan, L.S. Fan, J.L. Gong, Metal oxide redox chemistry for chemical looping processes, Nat. Rev. Chem. 2 (2018) 349–364.
[45] F. Wang, J. Graetz, M.S. Moreno, C. Ma, L.J. Wu, V. Volkov, Y.M. Zhu, Chemical distribution and bonding of lithium in intercalated graphite: identification with optimized electron energy loss spectroscopy, ACS Nano 5 (2011) 1190–1197.
[46] J.K. Norskov, T. Bligaard, J. Rossmeisl, C.H. Christensen, Towards the computational design of solid catalysts, Nat. Chem. 1 (2009) 37–46.
[47] H.X. Zhong, Q. Zhang, J. Wang, X.B. Zhang, X.L. Wei, Z.J. Wu, K. Li, F.L. Meng, D. Bao, J.M. Yan, Engineering ultrathin C_3N_4 quantum dots on graphene as a metal-free water reduction electrocatalyst, ACS Catal. 8 (2018) 3965–3970.
[48] Y. Qiao, J. Yi, S.C. Wu, Y. Liu, S.X. Yang, P. He, H.S. Zhou, Li-CO_2 electrochemistry: a new strategy for CO_2 fixation and energy storage, Joule 1 (2017) 359–370.